Journal of Sound and Vibration (2000) **231**(4), 1079–1110
doi:10.1006/jsvi.1999.2654, available online at http://www.idealibrary.com on IDEAL®

LOCATING STRUCTURAL DAMAGE BY DETECTING BOUNDARY EFFECTS

P. F. PAI AND S. JIN

Department of Mechanical and Aerospace Engineering, University of Missouri-Columbia, Columbia, MO 65211, *U.S.A.*

(*Received* 21 *June* 1999; *and in final form* 13 *September* 1999)

This paper presents a method of pinpointing structural damage locations using operational deflection shapes (ODSs) measured by a scanning laser vibrometer. The method assumes the form $C_1 \cos \beta x + C_2 \sin \beta x + C_3 \cosh \beta x + C_4 \sinh \beta x$ for an ODS to match with its experimental data using a sliding-window least-squares method to determine the four coefficients C_i. It is shown that C_1 represents the central solution of displacement, C_3 the boundary-layer solution of displacement caused by boundary constraints, $C_2\beta$ the central solution of slope, and $C_4\beta$ the boundary-layer solution of slope. Moreover, $C_1 * C_3$ is proportional to the difference of kinetic and elastic energy densities, $C_3 - C_1$ is proportional to the curvature, and $C_4 - C_2$ is proportional to the spatial derivative of the curvature. Because cracks on a structure introduce new boundaries to the structure and these coefficients change significantly at boundaries, crack locations are clearly revealed by the peaks on the $C_1 * C_3$ curve, sign change of C_4, peaks on the fitting error curve, and sudden changes of $C_3 - C_1$ and $C_4 - C_2$. Moreover, numerical and experimental results show that each of these coefficients requires a different length of data points for curve fitting in order to smooth the curve. Based on this different data length requirement and the peaks and sign change of these coefficients we derive a boundary effect detection (BED) method for finding damage locations. A non-linear sliding-window least-squares fitting technique is also derived for estimating the extent of structural damage. Numerical and experimental studies on beams with different damages have been performed to prove the accuracy and reliability of the BED method.

1. INTRODUCTION

Structural health monitoring research can be categorized into the following four levels: (I) detecting the existence of damage, (II) finding the location of damage, (III) estimating the extent of damage, and (IV) predicting the remaining fatigue life. The performance of tasks of Level (III) requires refined structural models and analyses, local physical examination, and/or traditional non-destructive evaluation (NDE) techniques. To perform tasks of Level (IV) requires material constitutive information on a local level, materials aging studies, damage mechanics, and high-performance computing. Levels (III) and (IV) are not the interest of this work. Many research tasks of Level (I) have been performed and the feasibility

0022-460X/00/141079 + 32 $35.00/0

was shown [1], but only few tasks of Level (II) have been done. To move the structural safety inspection from an expensive routine-based level to an economical condition-based level, a reliable systematic method for finding structural damage is required.

There are a wide variety of NDE techniques presently in use, including many ultrasonic methods, magnetic flux leakage inspection, radiography, dye penetration, and eddy current sensing. These methods are "local" methods; they can only find flaws in one small vicinity. They often require a skilled technician to scan the test object and to interpret results. Thus, the inspection of a large test object using such conventional NDE techniques is a costly and time-consuming process. This situation occurs only if the object is critical and a precise flaw resolution is necessary. To provide rapid inspection of large structures with minimal interruption of operations, "global" inspection methods are necessary instead of "local" conventional NDE methods. However, because global inspection methods are usually poor at locating or sizing flaws, necessary conventional NDE tests can be followed if the global inspection method issues a warning. Hence, global inspection methods should be regarded as a complement to standard NDE techniques, not a replacement.

Most structural health monitoring methods under current investigation focus on using dynamic responses to detect and locate damage because they are global methods that can provide rapid inspection of large structural systems [1]. These dynamics-based methods can be divided into four groups: (1) spatial-domain methods, (2) modal-domain methods, (3) time-domain methods, and (4) frequency-domain methods. Spatial-domain methods use changes of mass, damping, and stiffness matrices to detect and locate damage. Modal-domain methods use changes of natural frequencies, modal damping ratios, and mode shapes to detect damage. Time-domain methods use changes of the relationship between the input and output time signals to detect damage. Frequency-domain methods use changes in frequency responses functions (FRFs) or transmittance functions (TFs) to detect damage [2–4]. Moreover, one can use model-independent methods or model-referenced methods to perform damage detection using dynamic responses presented in any of the four domains. Literature shows that model-independent methods can detect the existence of damage without much computational efforts, but they are not accurate in locating damage. On the other hand, model-referenced methods are generally more accurate in locating damage and require fewer sensors than model-independent techniques, but they require appropriate structural models and significant computational efforts. Although time-domain methods use original time-domain data measured using conventional vibration measurement equipment, they require certain structural information and massive computation and are case sensitive [5]. On the other hand, frequency- and modal-domain methods use transformed data, which contain errors and noise due to transformation. Moreover, the modelling and updating of mass and stiffness matrices in spatial-domain methods are problematic and difficult to be accurate.

It is well known that measured structural dynamic responses are always contaminated by harmless uncertain conditions, which include input force noise,

material composition uncertainty, geometric variation, temperature, moisture, load uncertainty, and sensor noise. Hence, finding the damage after its possible existence is detected is necessary for preventing false alarms caused by these harmless effects.

Fracture mechanics research shows that, in most applications, there is a certain crack size at which a crack will grow spontaneously, and this size is typically of the order of millimeters and is usually less than 1 cm in length. According to the NDI Validation Center at Sandia National Laboratories, the size of cracks required to be detected in aircraft structures using non-destructive detection methods is 0.05" (1.27 mm) for main structures and 0.2" (5.08 mm) for substructures. Unfortunately, lower-mode structural frequencies are not sensitive to such small cracks because of small curvatures [6, 7]. Hence, low-frequency dynamic responses can be used to identify only large cracks. On the other hand, higher-mode frequencies are sensitive to small cracks because of high curvatures, and the change of strain energy (or curvature) distribution is also very localized, which provides a possibility for detecting small cracks. Hence, to detect small cracks using structural dynamic responses, high-frequency excitation is necessary in order to reduce the wavelength, to increase curvatures, and to activate the widening of cracks. However, measurement of high-frequency deformation shapes require spatially dense and accurate measurement. More seriously, the most popular structural modelling technique, the displacement-based finite-element method, is not accurate in predicting high-frequency responses because internal bending moments and shear forces are not formulated to be continuous at nodes. Hence, an accurate model-independent damage detection method with high-density measurement is really necessary for practical use.

To increase the density and accuracy of measurement, the Polytec PI PSV-200 Scanning Laser Vibrometer (SLV) in the authors' laboratory provides a unique solution to this problem because of its non-contacting, dense, and accurate measurement capability. This work is to derive an accurate and robust spatial-domain method using only operational deflection shapes (ODSs) measured by the SLV to locate damage.

2. THEORETICAL BACKGROUND

Here we derive the theory proposed for locating damage to structures using experimental ODSs. An ODS is the deflection shape of a structure subjected to a single-frequency harmonic excitation. When the excitation frequency is close to an isolated natural frequency of the structure, the ODS is dominated by the corresponding mode shape. If it is not an isolated natural frequency, the ODS may consist of multiple mode shapes. To show the concept without complex derivations we consider one-dimensional structures (i.e., beams) and assume that the obtained ODS consists of only one mode shape.

For a beam the governing equation is given by

$$(EIw'')'' + c\dot{w} + m\ddot{w} = f(x,t), \tag{1}$$

where E is Young's modulus, I is the area moment of inertia, c is the damping coefficients, m is the mass per unit length, f is the distributed external load, x is the spatial co-ordinate, t is the time, w is the transverse displacement, $(\ )' \equiv \partial(\ )/\partial x$, and $\dot{(\ )} \equiv \partial(\ )/\partial t$. A mode shape W of a uniform beam is the free undamped deflection shape vibrating at a natural frequency ω and is given by

$$W(x) = C_1 \cos(\beta x) + C_2 \sin(\beta x) + C_3 \cosh(\beta x) + C_4 \sinh(\beta x), \quad \beta \equiv (m\omega^2/EI)^{1/4}, \tag{2}$$

where the coefficients C_i need to be determined using boundary conditions.

For a uniform cantilever beam, it can be shown that the ith mode shape is given by

$$W_i(x) = \cosh \beta_i x - \cos \beta_i x + C(\sin \beta_i x - \sinh \beta_i x),$$

$$C \equiv \frac{\cos \beta_i L + \cosh \beta_i L}{\sin \beta_i L + \sinh \beta_i L}, \tag{3}$$

where L is the beam length and β_i (also ω_i) is determined by the frequency equation

$$1 + \cos \beta_i L \cosh \beta_i L = 0. \tag{4}$$

For a large $i(>2)$, Dugundji [8] showed that

$$\beta_i L = (i - 0.5)\pi, \quad C = 1 + 2(-1)^i e^{-\beta_i L} \simeq 1. \tag{5}$$

Hence, one can obtain that

$$W_i(x) = \sin \beta_i x - \cos \beta_i x + e^{-\beta_i x} - (-1)^i e^{-\beta_i (L-x)}, \quad i > 2. \tag{6}$$

To obtain linear extension, torsion, bending, and/or flexure solutions for isotropic beams, one commonly applies St. Venant's principle. St Venant's principle implies that the stresses at a point, which is sufficiently far from the loading end, depend only on the magnitude of the applied load and are practically independent of the manner in which the tractions are distributed over the end [9]. The deformations at points away from the ends where non-trivial stress resultants are applied are the so-called St. Venant solutions, or central solutions, or particular solutions [9, 10]. Moreover, St Venant's principle implies that a system of loads having zero resultant forces and moments (i.e., a self-equilibrated stress system) produces a displacement field that is negligible at a point far away from the loading end [9]. The displacements caused by such self-equilibrated loads at ends have short decay length and are called boundary-layer solutions, or extremity solutions, or eigensolutions, or transitional solutions [9, 10].

We note that the third and fourth terms in equation (6) are a sort of boundary-layer solutions because these two terms become zero when x is away from the left and right boundaries (i.e., $x = 0, L$). It indicates that $\cosh \beta x$ and $\sinh \beta x$ are due to boundary constraints, and $\cos \beta x$ and $\sin \beta x$ are central solutions [9]. Inspired by this observation we use these four functions to fit the experimental ODSs. However, because $\cosh \beta x$ and $\sinh \beta x$ may cause overflow problems, we will use a moving coordinate $\bar{x}$. Hence, ODSs are assumed to have the form

$$W(\bar{x}) = C_1 \cos(\beta \bar{x}) + C_2 \sin(\beta \bar{x}) + C_3 \cosh(\beta \bar{x}) + C_4 \sinh(\beta \bar{x}), \quad \bar{x} \equiv x - x_m, \tag{7}$$

where x_m is the location of the observed point. To find coefficients C_i $(i = 1, 2, 3, 4)$ for the point at $\bar{x} = 0$ (i.e., $x = x_m$) we use the data points around $x = x_m$ to minimize the fitting error. If W_i denote $W(\bar{x}_i)$ and Y_i the experimental data at $\bar{x}_i$, we define the fitting error E_{rror} as

$$E_{rror} = \sum_{i=-N}^{N} \alpha_i (W_i - Y_i)^2, \tag{8}$$

where the total number of points used is $2N + 1$, and α_i is a weighting factor. The four equations to determine the four coefficients (C_i) are given by

$$\frac{\partial E_{rror}}{\partial C_i} = 0 \quad , \quad i = 1, 2, 3, 4 \, . \tag{9}$$

After C_i are determined, one can obtain W, W', W'', and W''' by using the following equations:

$$W(0) = C_1 + C_3, \quad W'(0) = (C_2 + C_4)\beta, \quad W''(0) = (-C_1 + C_3)\beta^2,$$

$$W'''(0) = (-C_2 + C_4)\beta^3. \tag{10}$$

From equations (10) and the observation on equation (6) we know that C_1 represents the central solution of displacement (at $x = x_m$), C_3 the boundary-layer solution of displacement caused by boundary constraints, $C_2\beta$ the central solution of slope, and $C_4\beta$ the boundary-layer solution of slope. Damage creates new boundaries to a structure and introduces new boundary-layer solutions to the structure. When there is no damage at a point of a uniform structure, C_3 and C_4 should be zero if the point is away from boundaries and the mode number is high. If C_3 and C_4 are not zero at a point away from boundaries or C_3 and C_4 show sudden change at any point, it implies that boundary conditions are changed due to damage and/or non-uniform material distribution at that point.

It follows from equations (10) and (2) that the maximum elastic energy (Π) per unit length is given by

$$\Pi = \tfrac{1}{2} EIW''(0)^2 = \tfrac{1}{2} EI(C_3 - C_1)^2\beta^4 = \tfrac{1}{2} m\omega^2(C_3 - C_1)^2. \tag{11}$$

Moreover, under steady-state harmonic vibration the maximum kinetic energy (K) per unit length is given by

$$K = \tfrac{1}{2} m(W(0)\omega)^2 = \tfrac{1}{2} m\omega^2(C_3 + C_1)^2. \tag{12}$$

Hence the difference between these two energy densities is

$$K - \Pi = 2m\omega^2 C_1 C_3. \tag{13}$$

In other words, C_1C_3 is proportional to the difference between kinetic and elastic energy densities. Hence, if there is no damage, $C_3 = 0$ and hence $K = \Pi = 0$ at a point away from boundaries. This is a phenomenon useful for identifying boundary layers and damage locations.

The β in equation (7) needs to be estimated before using the linear sliding-window least-squares method shown in equations (8) and (9). To determine β for a high-frequency deflection shape one can plot the experimental ODS and then pick up a representative wavelength λ to obtain $\beta = 2\pi/\lambda$. For a low-frequency deflection shape (e.g., $i < 3$), it is difficult to obtain an accurate estimation of β from the ODS. However, one can use the theoretical value of a beam with boundary conditions similar to the one under study. It is shown later that, for finding damage locations, the proposed method does not require an accurate estimation of β. Moreover, if the estimated β is not correct, the sectional standard deviation of the curve-fitting and boundary-layer solutions will show periodic change. Hence, it is easy to know whether the estimated β is correct, and, if necessary, one can revise the estimation and rerun the signal processing. Furthermore, if necessary, one can use the non-linear sliding-window least-squares method shown in Appendix A to find β and C_i simultaneously. After β is computed using the non-linear curve fitting, one can estimate the change of m/EI (see equation (2)) to quantify the damage. However, it is shown later that computation of β requires a large sliding-window length (i.e., large N) in order to have a converged solution. Moreover, one must know that non-linear curve fitting requires iteration, which is computationally expensive.

3. NUMERICAL AND EXPERIMENTAL RESULTS

Damage detection is an inverse problem; it is difficult to obtain a unique solution. Considering both solution non-uniqueness and experimental noise at the same time will make it very difficult to develop damage detection methods. Here we first perform studies using numerical data without noise to get a clear idea of what

parameters are sensitive to damage in the proposed method. Then we add normally distributed random noise to the data to check the robustness of the method. In order to simulate dynamics of beams with cracks, we present the modelling and dynamic characteristics of beams with cracks next.

3.1. DYNAMIC CHARACTERISTICS OF BEAMS WITH CRACKS

To perform numerical study of the proposed damage detection method, we consider a $17.875'' \times 0.996'' \times 0.124''$ cantilevered copper beam with a symmetric, open crack at $x = a$, as shown in Figure 1. The free undamped equation of this can be derived to be

$$[E(I - \hat{I})w'']'' + m\ddot{w} = 0, \tag{14}$$

where

$$\hat{I} \equiv I_1 [u(x - a) - u(x - a - c)], \quad I_1 \equiv 2 \int_{h/2-d}^{h/2} z^2 \, \mathrm{d}A. \tag{15}$$

Here, A is the cross-sectional area, $u(x - a)$ is a unit step function, and d and c are the depth and width of the crack. Equation (14) shows that the existence of a crack redistributes the bending stiffness, especially around the crack-tip region [6, 7]. Equation (14) can be rewritten as

$$EIw^{iv} + m\ddot{w} = EI_1 w''[u''(x-a) - u''(x-a-c)] + 2EI_1 w'''[u'(x-a) - u'(x-a-c)]$$
$$+ EI_1 w^{iv}[u(x-a) - u(x-a-c)]. \tag{16}$$

Equation (16) shows that the free undamped vibration of a beam with a crack is equivalent to an intact beam subjected to two concentrated bending moments $EI_1 w''$ and two concentrated shear forces $2EI_1 w'''$ at $x = a$ and $x = a + c$ and one distributed force $EI_1 w^{iv}$ between $x = a$ and $x = a + c$. Man *et al.* [6] solved equation (16) using the Laplace transformation by following the approach used by Thomson [11]. We repeated the process and solutions and found that this method gives acceptable mode shapes but cannot give accurate natural frequencies. For example, the second natural frequency of a clamped–clamped beam should not decrease due to the presence of a symmetric open crack at the center, but this method cannot have such a prediction.

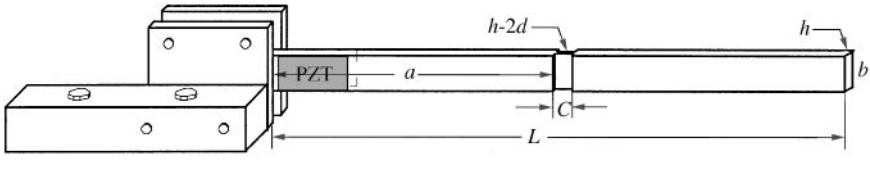

Figure 1. A cantilevered copper beam with a symmetric open crack and two integrated PZT patches for vibration measurement.

Christides and Barr [12] developed a model of cracked beams based on fracture mechanics, which requires a correction factor to be determined by matching analytical results with experimental results. The correction factor is the exponential coefficient of a crack function that is maximum at the crack tip and decays exponentially from the crack along the longitudinal direction. Moreover, Cawley and Adams [13] showed that the predicted dynamic responses using a slot in the modelling to represent a crack in the actual structure agree with experimental results. Hence we will model the beam in Figure 1 as three separate beam segments, and a correction factor k will be used to account for the stress concentration around the slot. The bending stiffness ($E(I - I_1)$) of the slotted section is modified to be $kEb(h - 2d)^3/12$. The value of k highly depends on the geometry of the crack tip. The ith mode shape of the jth beam segment is presented as

$$\hat{W}_j(x) = A_j \cos \beta_j x + B_j \sin \beta_j x + C_j \cosh \beta_j x + D_j \sinh \beta_j x. \tag{17}$$

Each beam segment has its own β_j but there is only one ith natural frequency. Because of the use of hyperbolic functions $\cosh \beta x$ and $\sinh \beta x$, the origin of x is set at the center of each beam segment to reduce the chance of numerical singularity. Using the boundary conditions and continuity of displacements, slopes, bending moments, and shear forces, one can solve for β_j for each beam segment and the ith natural frequency.

Figure 2 shows the first 10 intact mode shapes compared with the ones with a crack at the center. The total crack depth (i.e., $2d$) is 60% of the beam thickness, the crack width is 0.05″ (i.e., $c/L = 0.28\%$), and $k = 0.4$ is assumed. It is a big crack.

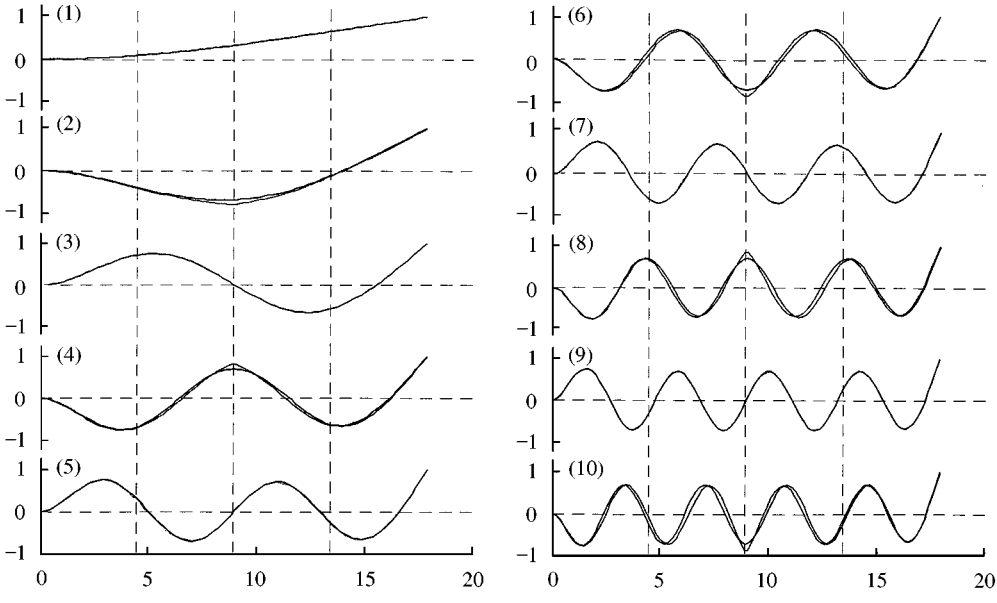

Figure 2. The first 10 intact mode shapes and the mode shapes with a center crack, where $a + c/2 = 0.5L$, $c = 0.05''$, $d = 0.3h$, and $k = 0.4$.

We note that the crack does not have significant influence on Modes 1, 3, 5, 7, and 9 because the curvatures of these modes are almost zero at the center. For high-frequency modes, the nodes (fixed points) move toward the crack location, but the shapes do not change except around the crack. Figures 3(a) and 3(b) show the variation of the first 10 natural frequencies with the depth of a crack at $x = 0.2L$ and $x = 0.8L$, respectively. We note that lower-mode frequency ratios drop dramatically when the crack depth increases. It reveals that deep cracks have significant influence on low-frequency modes. Moreover, the depth and location of a crack have more influence on lower-mode frequencies than on higher-mode

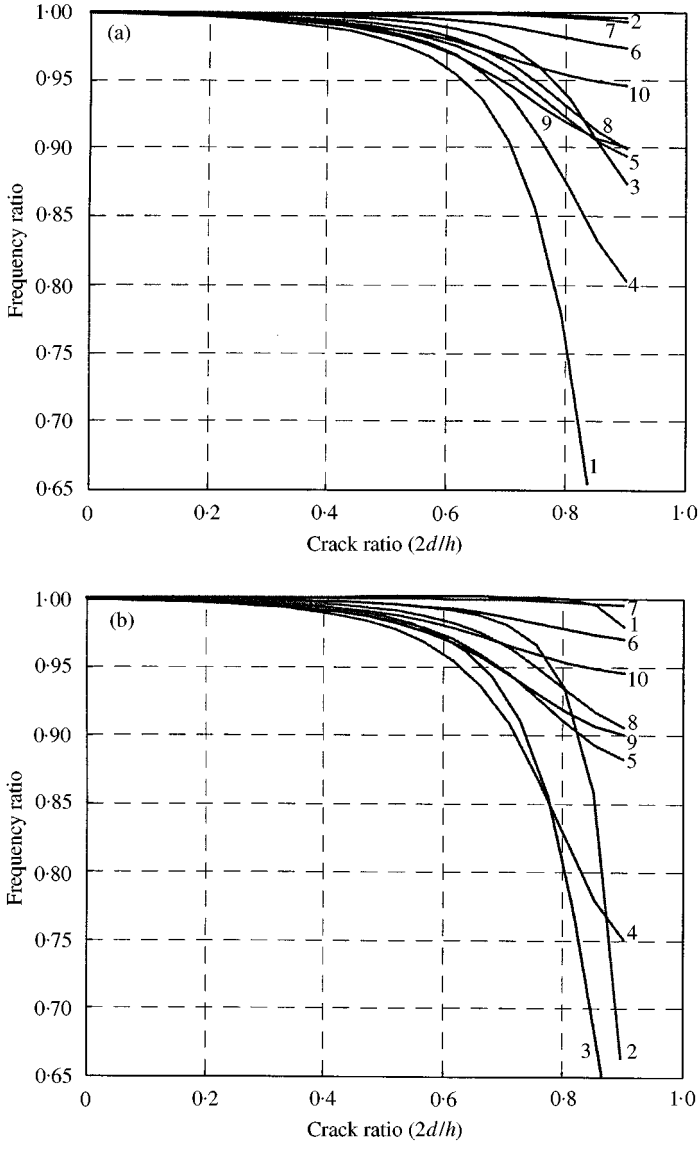

Figure 3. The influence of crack depth on the first 10 natural frequencies: (a) $a + c/2 = 0.2L$ and $c = 0.05''$, and (b) $a + c/2 = 0.8L$ and $c = 0.05''$.

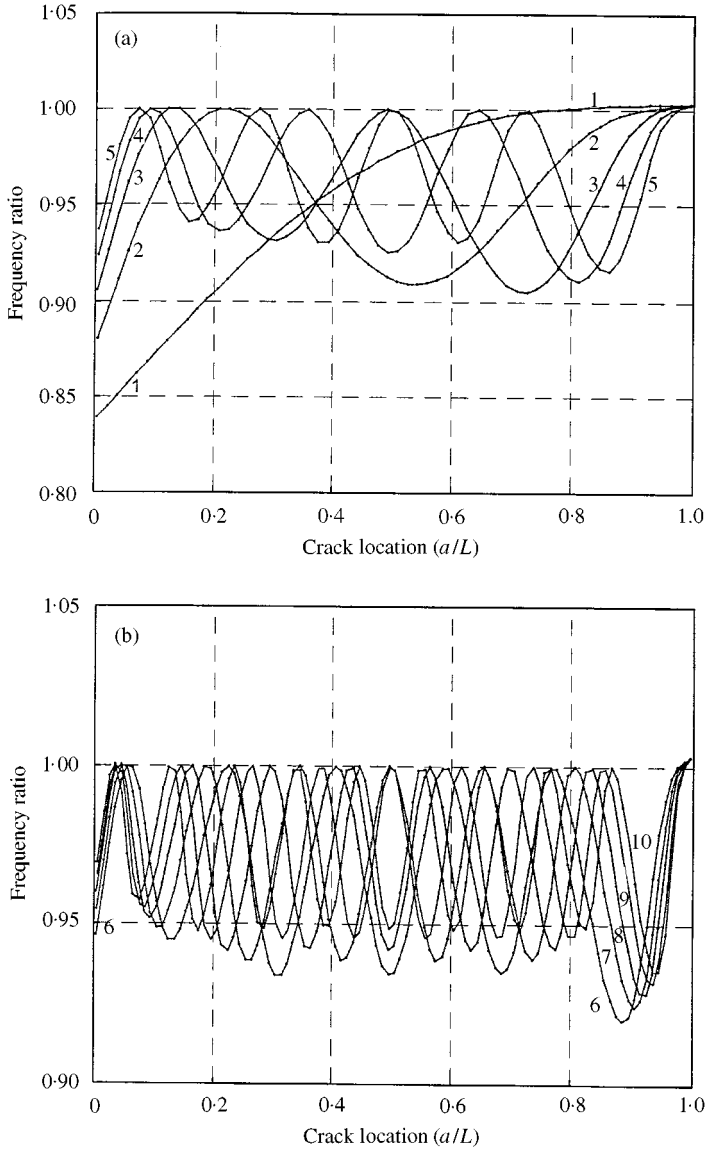

Figure 4. The influence of the location of a crack with $c = 0.05''$ and $d = 0.3h$ on natural frequencies: (a) the first to fifth natural frequencies, and (b) the sixth to 10th natural frequencies.

frequencies. Figure 4 shows how the crack location affects the first 10 natural frequency ratios. It also shows that a crack reduces the higher-mode frequency ratios to a lesser extent. Figure 5 shows how the crack width of a center crack changes the first 10 frequency ratios. We note that some natural frequencies saturate after the crack width increases beyond 1% of L.

In the literature, some researchers study the use of natural frequency shift in FRFs to detect structural damage. To see the influence of cracks on FRFs, we compute the frequency response function H_{mn} using the following

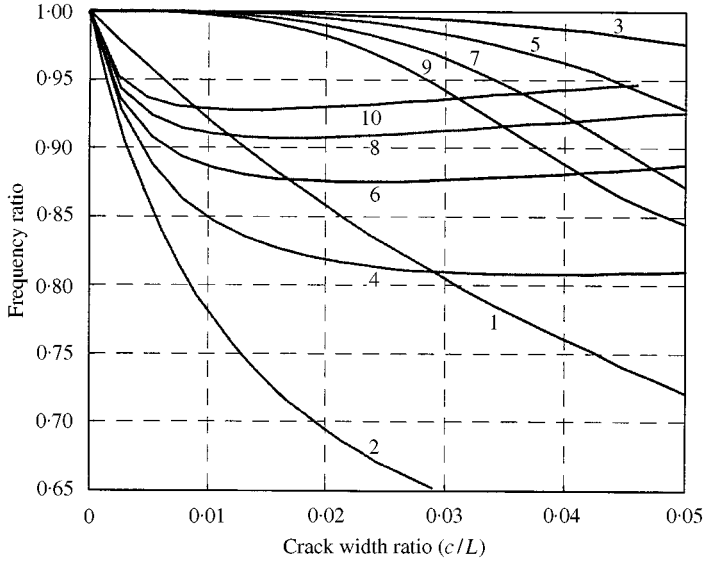

Figure 5. The influence of the width of a center with $d = 0.3h$ on the first 10 natural frequencies.

equation [14]:

$$H_{mn}(\Omega) = \sum_{i=1}^{\infty} \frac{\phi_{im}\phi_{in}}{\omega_i^2 - \Omega^2 + 2\xi_i\omega_i\Omega j}, \tag{18}$$

where ϕ_{im} denotes the value of the ith eigenfunction ϕ_i at $x = x_m$, ω_i is the ith undamped natural frequency, and ξ_i is the ith modal damping ratio. Here, the eigenfunctions are normalized such that $\int_0^L \phi_i m \phi_i \, dx = 1$.

The natural frequencies of the copper beam in Figure 1 are experimentally obtained using two PZT (lead zirconate titanate) patches attached to the root of the beam; one is to excite the beam and the other is to sense the vibration. The first five natural frequencies are experimentally obtained by sweeping the excitation frequency to be 9.590, 59.51, 164.8, 319.9, and 524.9 Hz, which are very close to the theoretical ones obtained from the Euler–Bernoulli theory. Each modal damping ratio is obtained by exciting the specific mode under study and then using the Hilbert transformation to extract the damping ratio from the free, damped response. The first five modal damping ratios are obtained to be 0.22, 0.11, 0.12, 0.10 and 0.10%. All other modal damping ratios will be assumed to be 0.10% in using equations (18). The mass density ρ is measured to be 0.272 lb/in^3, and Young's modulus E is derived to be 1.542×10^7 psi by minimizing the difference between the measured third and fifth natural frequencies and the theoretical ones.

Figures 6(a) and 6(b) show the $|H_{64}|$ (response at $x = 0.6L$, excitation at $x = 0.4L$) of the beam with a crack at $x = 0.2L$ and $x = 0.8L$ respectively, compared with the intact ones, where 20 modes are used in equation (18). The stars indicate the peak values at the exact natural frequencies. We note that the natural

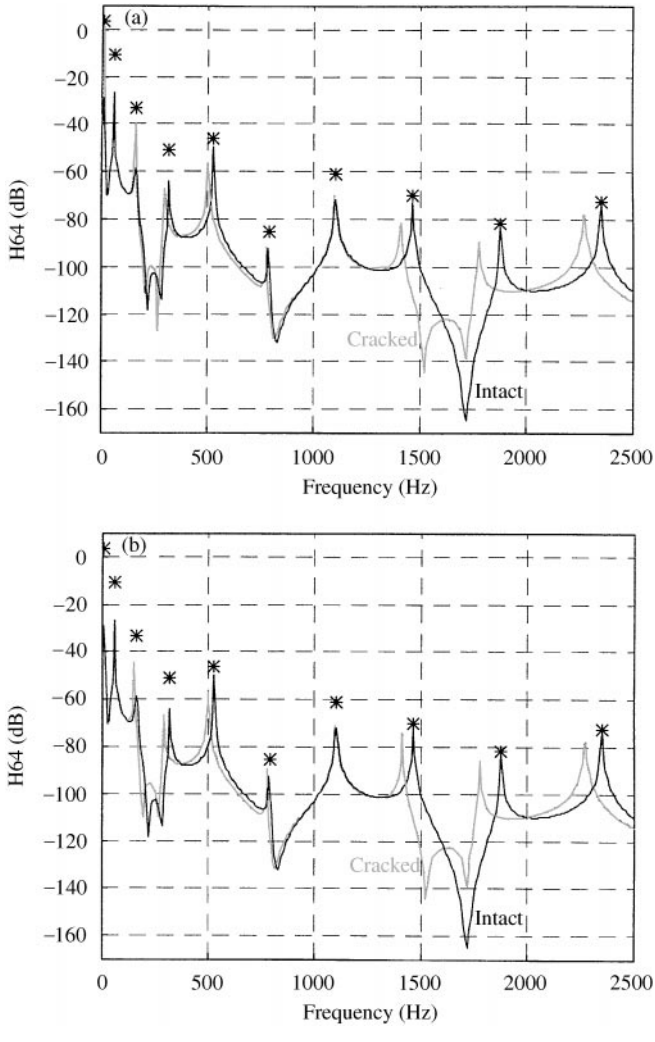

Figure 6. The FRFs of the intact beam and the beam with a crack having $c = 0.05''$, $d = 0.3h$, and $k = 0.4$ at (a) $a + c/2 = 0.2L$, and (b) $a + c/2 = 0.8L$.

frequencies are apparently shifted because the assumed crack is large. However, the FRF does not change around the natural frequencies of Modes 1, 3, 5, 7, and 9 because the modes are not affected by the crack as shown in Figure 2. We note that the crack location has greater influence on the FRFs around low-frequency areas, which reveals the same trend observed in Figure 3.

3.2. EXPERIMENTAL SET-UP AND PROCEDURES

Figure 7 shows the experimental set-up used in measuring ODSs of structures. A Polytec PI PSV-200 Scanning Laser Vibrometer (SLV) is used to measure the

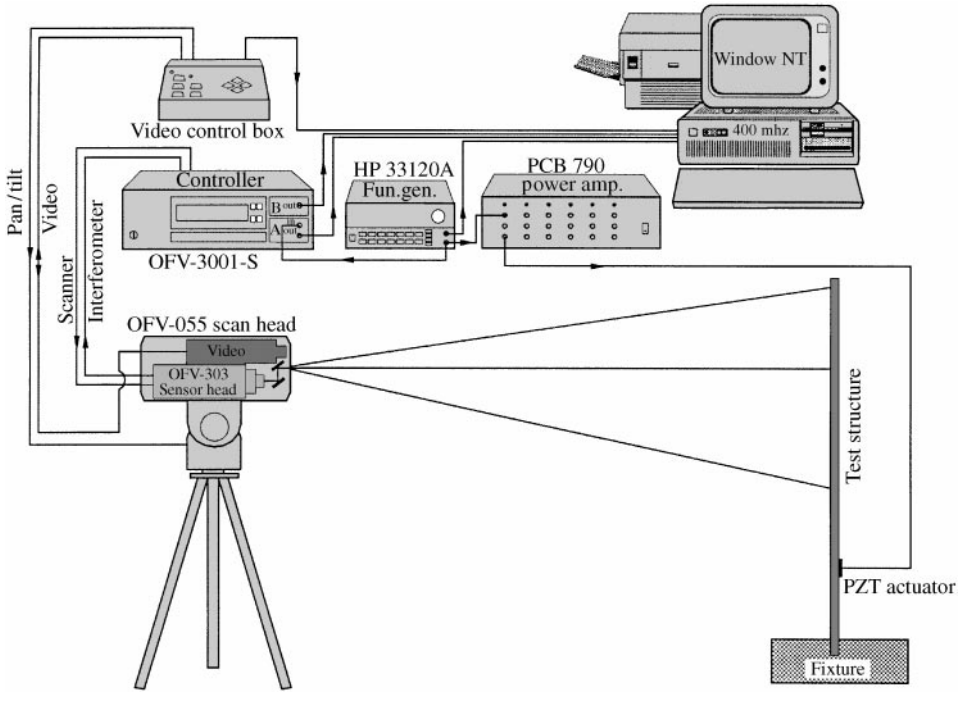

Figure 7. The experimental set-up for measuring operational deflection shapes of a cantilevered beam using a PSV-200 scanning laser vibrometer and a PZT patch.

velocities of 200 or 250 or 400 equally spaced points along a beam, and the PZT is attached to the root of the beam to excite the structure. The PZT patch is a QuickPack QP10N actuator purchased from the ACX [15]. The QuickPack actuator packages piezoceramics in a protective skin (a polyimide coating) with pre-attached electrical leads. It makes fragile piezoceramics much easier to work with and easier to integrate into the structure. The size of QP10N is $2'' \times 1'' \times 0.015''$, and its piezo wafer size is $1.81'' \times 0.81'' \times 0.010''$. The input voltage to the PZT patch is used as the reference signal in data acquisition, and the maximum operating voltage is 200 V.

In the experiment, we first perform an "FFT" acquisition to obtain FRFs using a periodic chirp excitation, and then we choose an isolated natural frequency from the averaged FRF. After that we perform a "FAST SCAN" acquisition using a single-frequency excitation at the chosen frequency to obtain the corresponding ODS.

The noise level of the measured ODSs is primarily determined by the frequency bandwidth B_w used in the "FAST SCAN" acquisition. The noise level is proportional to $\sqrt{B_w}$. However, the minimum bandwidth is 0.02% of the excitation frequency, and the data acquisition time increases when B_w decreases. Hence, the noise level of high-frequency ODSs obtained using the "FAST SCAN" acquisition can be high. However, the ODSs obtained in this study are estimated to have a noise level below 1% of the measured amplitude.

3.3. RESULTS ON DAMAGE DETECTION

Here we show how to locate structural damage by examining the boundary effects revealed by the coefficients obtained from the sliding-window least-squares fitting. We consider four cases. For each case we first present the numerical study, and then we show experimental results and compare them with the numerical prediction.

3.3.1 *Case* (1): *a cantilevered aluminium beam with a center crack*

Figure 8 shows a $24.125'' \times 0.743'' \times 0.188''$ aluminium beam with three cracks, which are actually narrow slots. The crack width is $c = 0.055''$. The Young modulus is experimentally determined to be $E = 9.15 \times 10^6$ psi, and the mass density is $\rho = 5.2$ slug/ft^3. Cracks $\#1$, $\#2$, and $\#3$ are cut in sequence, and they are about 28, 16 and 12% of the beam thickness, respectively. The beam with only Crack $\#1$ is named CASE (1) and the result is presented here.

Figure 9 shows the results of processing the analytical sixth mode shape with only Crack $\#1$, which is obtained using the method described in Section 3.1. We assumed $k = 0.6$ to account for the stress concentration, which may not be accurate but it will not affect our study of damage detection. The unit of ODSs is m/s, and W_m is the maximum value of the ODS. The sectional standard deviation SSD in the fitting process is computed as

$$SSD \equiv \sqrt{\frac{\sum_{i=-N}^{N} [W(\bar{x}_i) - Y(\bar{x}_i)]^2}{2N+1}}. \tag{19}$$

The overall standard deviation SD is computed after the C_i for every point on the beam are obtained, and it is computed as

$$SD \equiv \sqrt{\frac{\sum_{m=1}^{M} [W(x_m) - Y(x_m)]^2}{M}}, \tag{20}$$

where M is the total number of points measured on the beam. In Figure 9 we use no noise, $N = 5$, $\Delta x = L/100$ (the distance between two adjacent measuring points), and

$$\alpha_i = \frac{1}{1 + |99i/N|}. \tag{21}$$

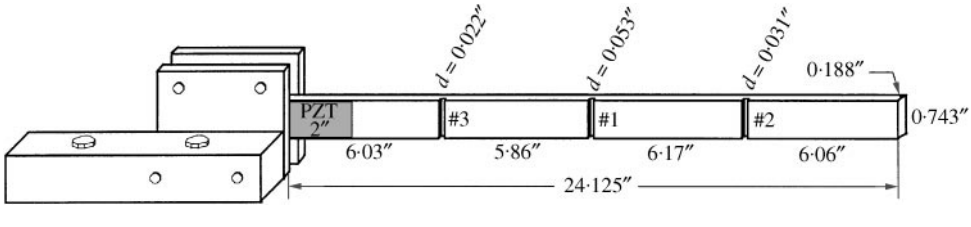

Figure 8. A cantilevered aluminum beam with three cracks.

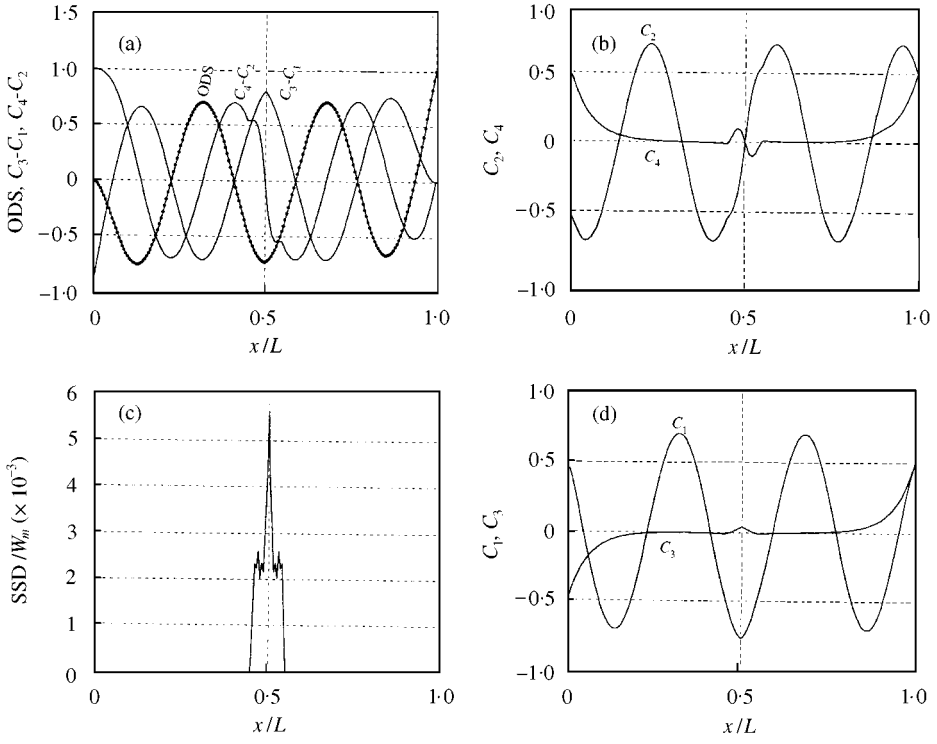

Figure 9. Numerical boundary effect detection of Crack #1 using the sixth mode shape as the ODS with $M = 200$, $N = 5$, and $\Delta x = L/100$: (a) ODS (dots), fitted ODS (solid line connecting dots), $C_3 - C_1$, and $C_4 - C_2$, (b) C_2 and C_4, (c) SSD/W_m, and (d) C_1 and C_3.

In Figure 9(a) it is impossible to detect the difference between the analytical mode shape (dots) and the curve-fitted shape (the solid line connecting the dots) because the overall standard deviation SD is 0.01% of W_m. We note that it is difficult to find the crack location from the mode shape. However, the sudden change on the $C_3 - C_1$ curve (i.e., W'', see equation (10)) and the $C_4 - C_2$ curve (i.e., W''') shows the area of damage, but not the precise location.

Figure 9(b) shows that, away from boundaries, the boundary-layer solution C_4 is zero except around the crack and it changes sign at the exact crack location. Moreover, Figure 9(d) shows that, away from boundaries, the boundary-layer solution C_3 is zero except around the crack and it has a peak at the exact crack location. Furthermore, one can see from Figure 9(c) that SSD has a peak at the crack location. Because the C_2 curve is wavy and its change around crack is not obvious, it is difficult to use C_2 in searching for damage location. Similarly, the change of C_1 around the crack is not obvious. However, because $C_1 * C_3$ is proportional to the difference between the kinetic and elastic energies as shown in equation (13), it is more meaningful to use $C_1 * C_3$ instead of C_3 in searching for damage.

Harmonic functions are not orthogonal to hyperbolic functions, and $\int_0^X \sin \beta x \cos \beta x \, dx$ is zero only if $X = 2\pi n/\beta$. To accurately separate central

solutions from boundary-layer solutions using the sliding-window least-squares fitting method proposed here, one needs to choose an appropriate number of points (i.e., N) to enforce the orthogonality in order to obtain accurate values for C_i to separate central and boundary-layer solutions. To have the orthogonality, $2N\Delta x$ need to cover an integer number of the wavelength λ of $\cos \beta x$. However, to use the appearance of boundary-layer solutions to locate the damage one does not need to choose $2N\Delta x$ to cover an integer number of λ. But, when $2N\Delta x$ does not cover an integer number of λ, the obtained C_1 and C_3 may not really represent the central solutions. This is the reason why the C_2 curve in Figure 9(b) is distorted from the sine curve as it should be. However, the distortion of C_2 causes C_4 to have significant change at the crack location, and it is useful for locating damage. The same phenomenon occurs for C_1 and C_3.

In real cases, these nice features for pinpointing crack locations are affected by experimental noise in different degrees. Figure 10 shows the same case presented in Figure 9 except that we add to the mode shape a normally distributed random noise with a standard deviation of 0.2% of W_m. To show the influence of the sliding-window length used in the curve fitting, we increase Δx from $\Delta x = L/100$ in Figure 10 to $\Delta x = 3L/200$ in Figure 11, and to $\Delta x = L/50$ in Figure 12. From Figures 10–12 we note that, similar to C_3, $C_1 * C_3$ has a peak at the crack location

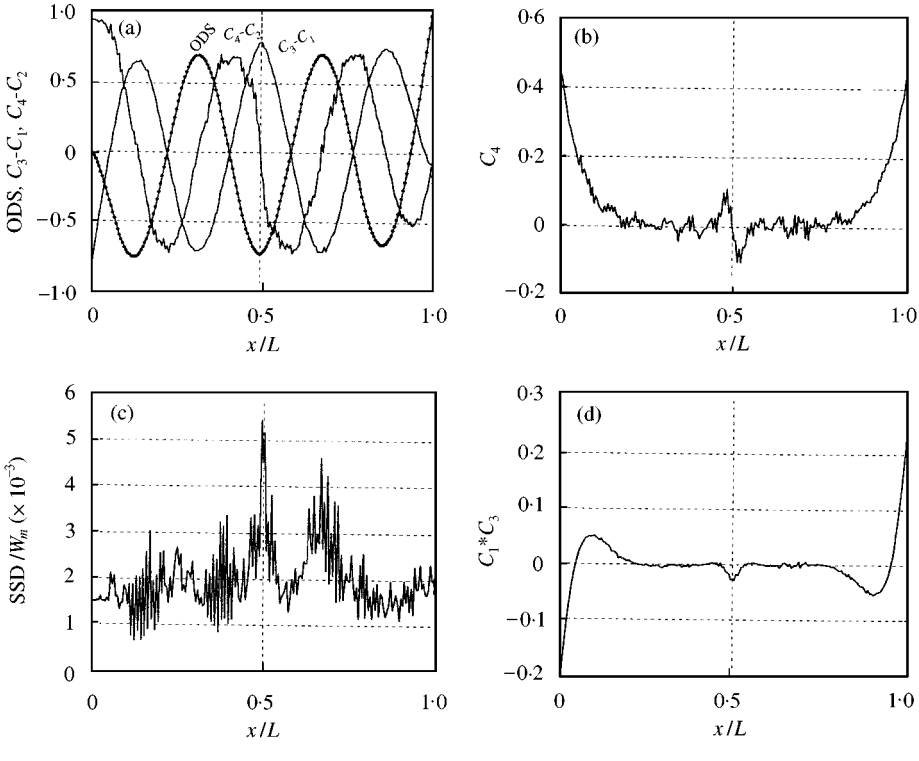

Figure 10. Numerical boundary effect detection of Crack #1 using the sixth mode shape with 0.2% noise and $M = 200$, $N = 5$, and $\Delta x = L/100$: (a) ODS (dots), fitted ODS, $C_3 - C_1$, and $C_4 - C_2$, (b) C_4, (c) SSD/W_m, and (d) $C_1 * C_3$.

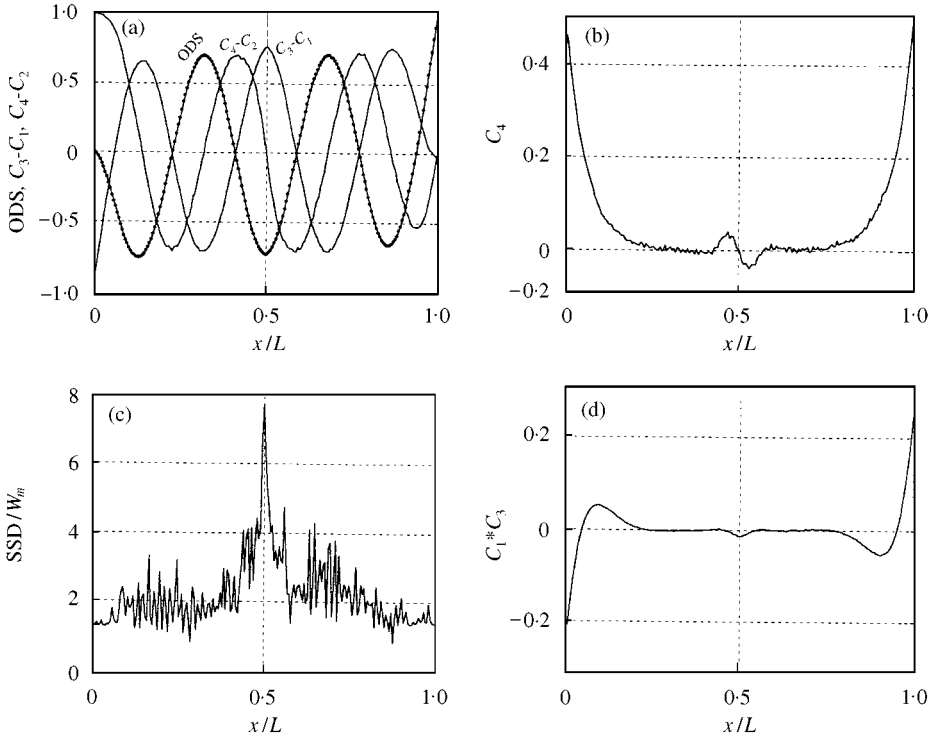

Figure 11. Numerical boundary effect detection of Crack #1 using the sixth mode shape with 0.2% noise and $M = 200$, $N = 5$, and $\Delta x = 3L/200$: (a) ODS (dots), fitted ODS, $C_3 - C_1$, and $C_4 - C_2$, (b) C_4, (c) SSD/W_m, and (d) $C_1 * C_3$.

and the peak is more obvious if Δx is small. $C_3 - C_1$ requires about the same or a little bit larger Δx than $C_3 * C_1$ to smooth out the curve. Because C_2 is much larger than C_4 and C_2 is wavy, C_4 requires a little bit larger Δx than $C_4 - C_2$ to smooth out the curve. Furthermore, the sectional standard deviation SSD has a peak at the crack location only if Δx is large, and the peak is not as obvious as the one of $C1 * C3$. We note that, when the sliding-window length $2N\Delta x$ is short, the C_i curves are rough, which may make is difficult to locate the damage. On the other hand, when $2N\Delta x$ is large the boundary-layer effects around the crack are averaged out and it is also difficult to locate the damage. However, because every C_i requires a different window length and shows the crack location in a different way, one can perform a series of analysis using different window lengths and then search for the damage using these series of results.

The peak of $C_1 * C_3$ indicates that the kinetic energy is less than the elastic energy around the crack. Because m and EI are assumed to be constant in the signal processing, the actual large curvature around the crack causes the estimated elastic energy to be high and hence $K - \Pi < 0$.

Figures 13–15 show the results of processing the ODS corresponding to the sixth mode of the beam shown in Figure 8 with only Crack #1. In the "FAST SCAN" acquisition, the laser beam measures the vibration velocities of points on the beam's

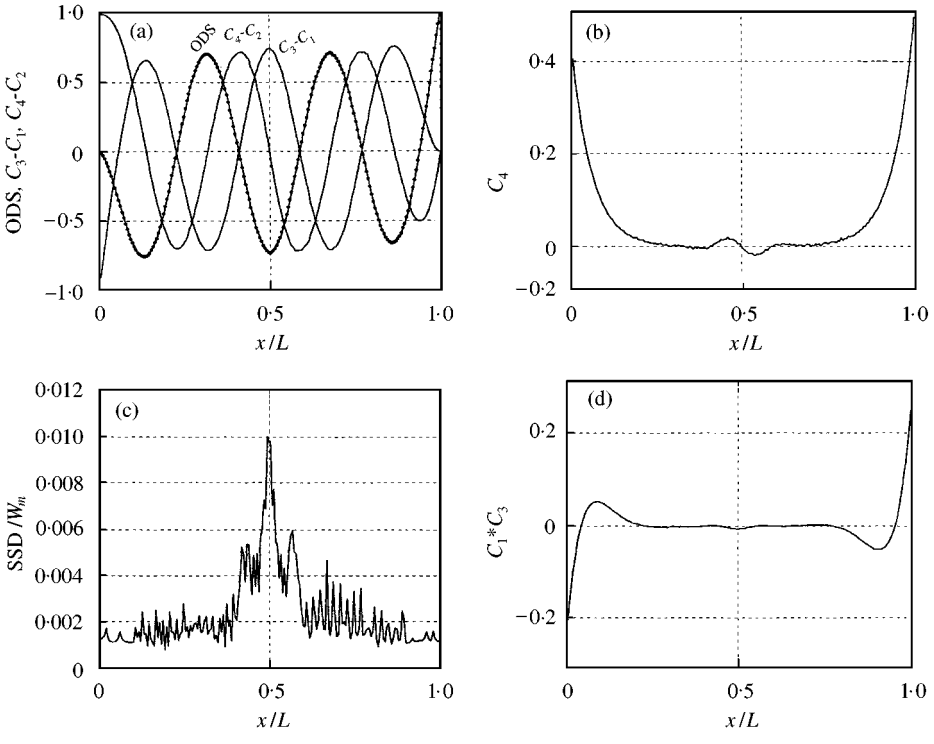

Figure 12. Numerical boundary effect detection of Crack #1 using the sixth mode shape with 0.2% noise and $M = 200$, $N = 5$, and $\Delta x = L/50$: (a) ODS (dots), fitted ODS, $C_3 - C_1$, and $C_4 - C_2$, (b) C_4, (c) SSD/W_m, and (d) $C_1 * C_3$.

backside, the PZT patch is excited by $100 \sin(1668.8\,\pi t)$ V, and the frequency bandwidth is chosen to be 8.344 Hz. The excitation frequency is 834.4 Hz, which is the sixth natural frequency from the averaged FRF obtained using the "FFT" acquisition. Because a frequency bandwidth of 5000 Hz is used in the "FFT" acquisition with 3200 FFT lines, the frequency resolution is 1.56 Hz. Crack #1 reduces the sixth natural frequency from 840.0 to 834.4 Hz according to the averaged FRF curve. We use $M = 200$ and $N = 5$ and $\Delta x = L/100$ in Figure 13, $\Delta x = 3L/200$ in Figure 14, and $\Delta x = L/50$ in Figure 15. We note that it is almost impossible to find the crack from the $C_3 - C_1$ and $C_4 - C_2$ curves in Figures 14(a) and 15(a). Although the $C_3 - C_1$ curve in Figure 13(a) shows the crack location, the $C_4 - C_2$ curve may confuse the reader with other possible cracks. On the other hand, the crack location can be easily identified from Figures 13(d), 14(b), 14(d), 15(b), and 15(c). To assure the locations of small cracks, one can check for the sign change of C_4, the peaks of $C_1 * C_3$ and SSD, and the non-smoothness of $C_3 - C_1$ and $C_4 - C_2$. Comprising Figures 11 and 12 with Figures 14 and 15 we note that they almost have the same curves. The values are different because the numerical mode shape is normalized to have a maximum value of one. We also note that the noise pattern shown in Figures 13(b, c) is not the same as the normally distributed random noise shown in Figures 10(b, c). Moreover, one can see from Figure 13(c)

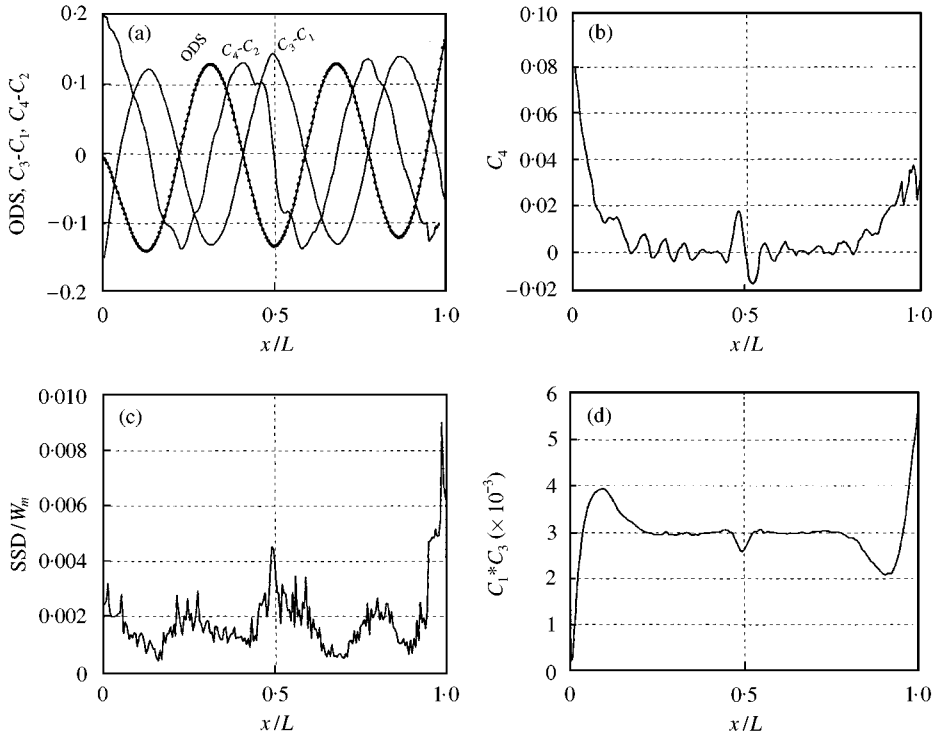

Figure 13. Experimental boundary effect detection of Crack #1 using the ODS corresponding to the sixth mode and $M = 200$, $N = 5$, and $\Delta x = L/100$: (a) ODS (dots), fitted ODS, $C_3 - C_1$, and $C_4 - C_2$, (b) C_4, (c) SSD/W_m, and (d) $C_1 * C_3$.

that the signal contains more noise at the beam tip ($x/L = 1$), which is probably due to the large rotation angle and the backscattered laser light is weak and has more noise.

Because low-frequency ODSs have small W'' and W''' and their boundary-layer solutions spread across the whole structure, it is difficult to find cracks using low-frequency ODSs. We process the ODS obtained by exciting the PZT patch with 60 sin (125 πt) V and a frequency bandwidth of 1.25 Hz. Crack #1 reduces the second natural frequency from 63.13 to 62.50 Hz according to the averaged FRF. Figure 16 shows that, even when $N = 5$ and $\Delta x = 3L/200$ are used, the $C_3 - C_1$ and $C_4 - C_2$ curves are still rough and it is difficult to find the crack from them. However, the $C_1 * C_3$ curve has a local peak to indicate the crack location, but it is not as clear as the one in Figure 14 (use the same window length) because C_3 is non-zero everywhere. Smoothing of the curves requires a long window length, but it will average out the boundary effect and makes it impossible to find the crack.

3.3.2. *Case* (2): *a cantilevered aluminium beam with two cracks*

One can see from Figures 2 and 8 that Crack #2 is very close to one of the nodes of the sixth mode. Hence, it is difficult to detect Crack #2 using the ODS

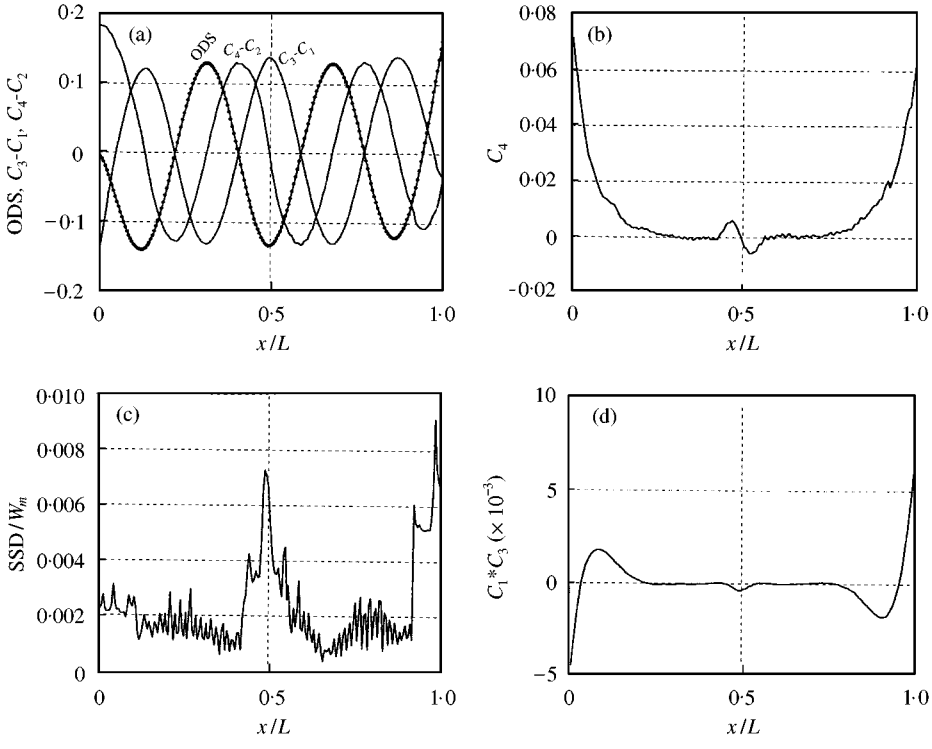

Figure 14. Experimental boundary effect detection of Crack #1 using the ODS corresponding to the sixth mode and $M = 200$, $N = 5$, and $\Delta x = 3L/200$: (a) ODS (dots), fitted ODS, $C_3 - C_1$, and $C_4 - C_2$, (b) C_4, (c) SSD/W_m, and (d) $C_1 * C_3$.

corresponding to the sixth mode. Hence, we examine the ODS corresponding to the eighth mode. Cracks #1 and #2 reduce the eighth natural frequency from 1551 to 1544 Hz according to the averaged FRF, where a frequency resolution of 3.125 Hz is used. In the "FAST SCAN" acquisition, the PZT patch is excited by 20 sin (3088 πt) V, and the frequency bandwidth is chosen to be 15.44 Hz.

The experimental results of the beam shown in Figure 8 with Cracks #1 and #2 are shown in Figures 17 and 18. We use $N = 5$ and $\Delta x = 3L/400$ in Figure 17 and $\Delta x = L/100$ in Figure 18. The locations of Cracks #1 and #2 are very clear, especially from the peaks of $C1 * C_3$ and the sign changes of C_4. Because Crack #2 is smaller than Crack #1, it is not right on the peak of the ODS, and it is close to the boundary, the peaks of Crack #2 in Figures 17(b, d) and 18(b, d) are smaller than those of Crack #1. However, a crack with large peaks on C_4 and $C_1 * C_3$ curves may not really mean a large crack because it depends on the specific ODS under examination and the crack location.

3.3.3. *Case* (3): *a cantilevered aluminium beam with three cracks*

The experimental results of the beam shown in Figure 8 with Cracks #1, #2, and #3 are shown in Figures 19 and 20. The three cracks reduce the eighth natural

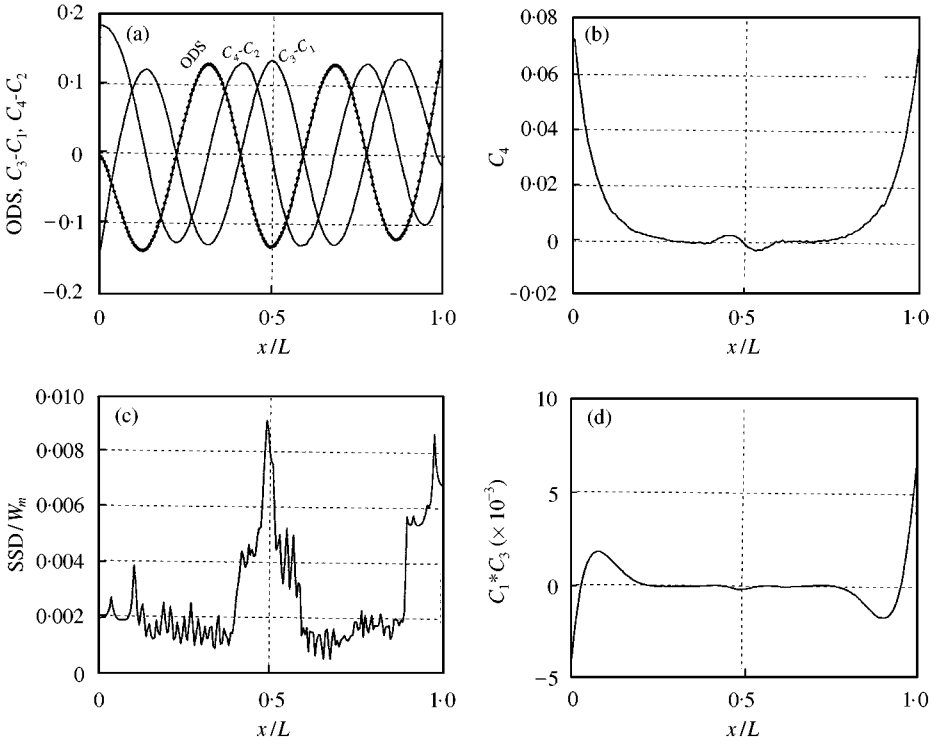

Figure 15. Experimental boundary effect detection of Crack #1 using the ODS corresponding to the sixth mode and $M = 200$, $N = 5$, and $\Delta x = L/50$: (a) ODS (dots), fitted ODS, $C_3 - C_1$, and $C_4 - C_2$, (b) C_4, (c) SSD/W_m, and (d) $C_1 * C_3$.

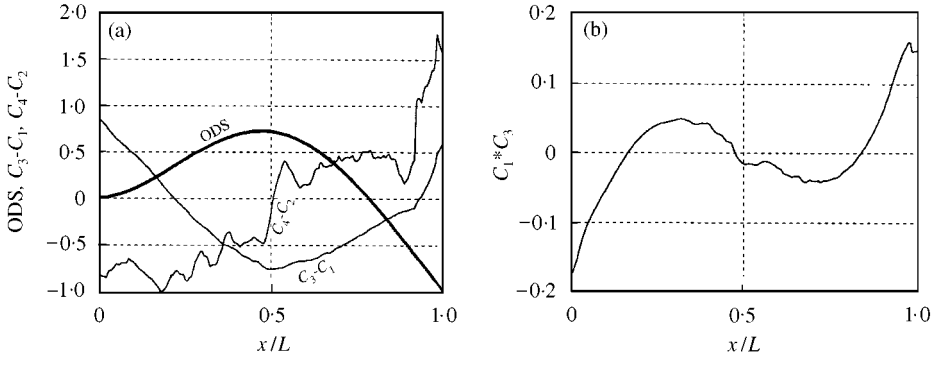

Figure 16. Experimental boundary effect detection of Crack #1 using the ODS corresponding to the second mode and $M = 200$, $N = 5$, and $\Delta x = 3L/200$: (a) ODS (dots), fitted ODS, $C_3 - C_1$, and $C_4 - C_2$, and (b) $C_1 * C_3$.

frequency from 1551 to 1529 Hz according to the averaged FRF, where a frequency resolution of 0.781 Hz is used. In the "FAST SCAN" acquisition, the PZT patch is excited by $140 \sin(3060\pi t)$ V, and the frequency bandwidth is chosen to be 1.53 Hz. We use $N = 5$ and $\Delta x = 3L/400$ in Figure 19 and $\Delta x = L/100$ in Figure 20. One

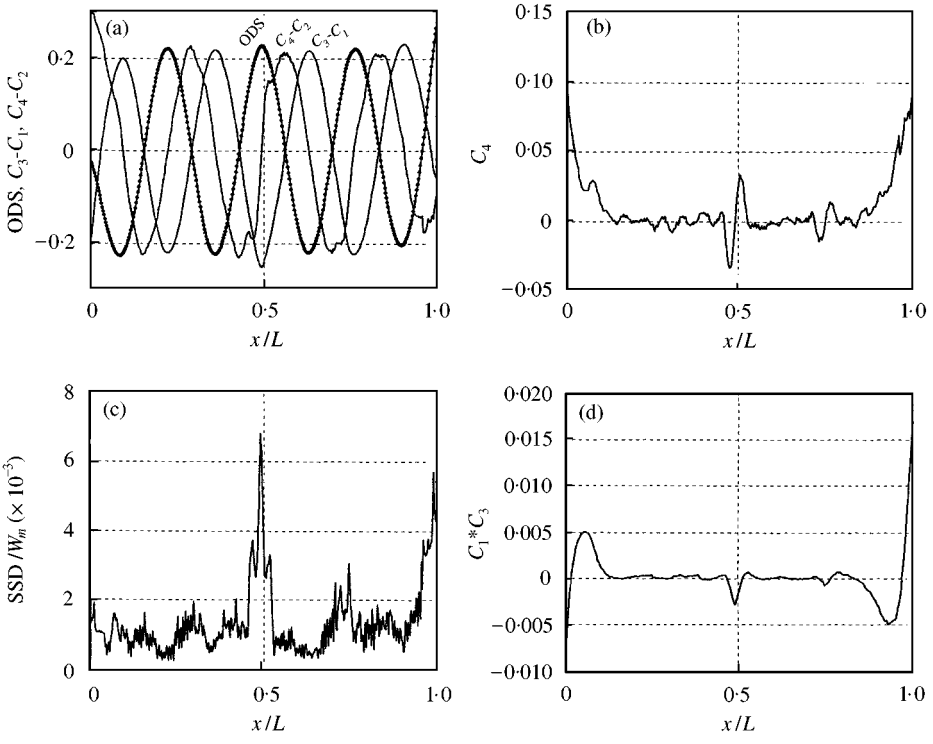

Figure 17. Experimental boundary effect detection of Cracks #1 and #2 using the ODS corresponding to the eighth mode and $M = 400$, $N = 5$, and $\Delta x = 3L/400$: (a) ODS (dots), fitted ODS, $C_3 - C_1$, and $C_4 - C_2$, (b) C_4, (c) SSD/W_m, and (d) $C_1 * C_3$.

can easily identify the locations of the three cracks, especially from the peaks of $C_1 * C_3$ and the sign change of C_4. Because Crack #3 is smaller than the other two cracks, the peak on the $C_1 * C_3$ curve is smaller. Because of experimental noise, the ODS amplitude needs to have a certain value in order to contain clear information of small cracks. But a high-frequency mode requires large power to have a certain amplitude. Moreover, the frequency bandwidth in the "FAST SCAN" acquisition is limited to 0.02% of the excitation frequency, but noise increases with the frequency bandwidth. To use very high-frequency ODSs to detect small cracks one needs to use the "LOCK-IN AMPLIFIER" acquisition to reduce the bandwidth and noise, and a high-power amplifier for PZT patches or other actuators is needed.

3.3.4. *Case* (4): *a copper beam with a short stiffened section*

Figure 21 shows the copper beam studied in Section 3.1 with an 1.83 lb steel block attached to the tip. This case is to show that this boundary effect detection method works for any boundary conditions and it can also be used to detect stiffness change in a structure. In the measurement we only scan the 15″ span

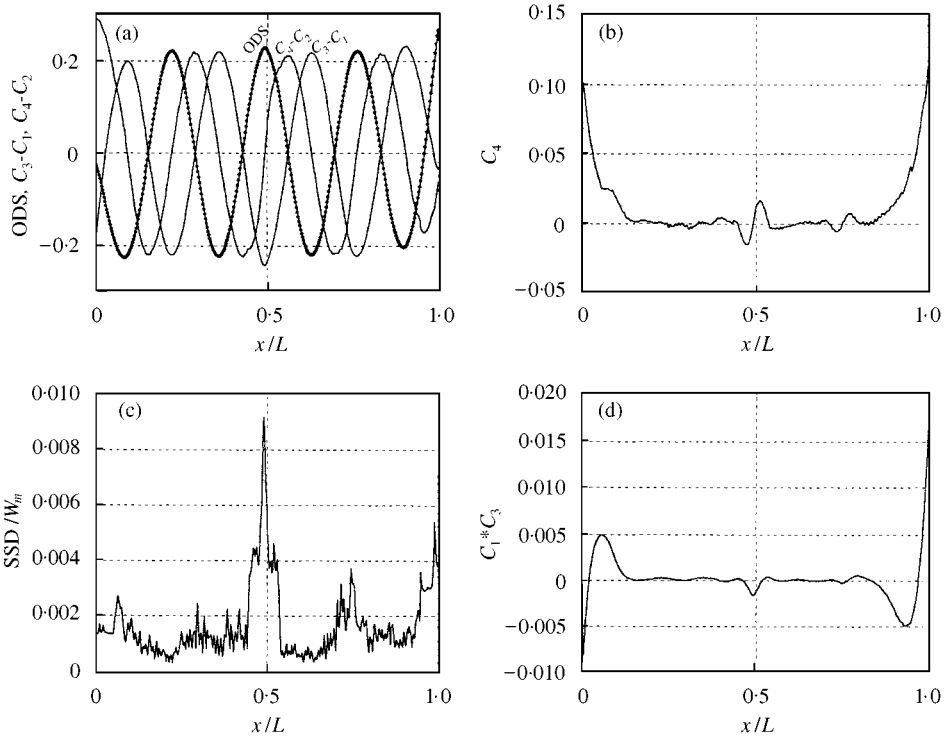

Figure 18. Experimental boundary effect detection of Cracks #1 and #2, using the ODS corresponding to the eighth mode and $M = 400$, $N = 5$, and $\Delta x = L/100$: (a) ODS (dots), fitted ODS, $C_3 - C_1$, and $C_4 - C_2$, (b) C_4, (c) SSD/W_m, and (d) $C_1 * C_3$.

of the back side from the right edge of the PZT patch to the left edge of the steel block.

To understand the results without experimental noise we perform the numerical simulation of a beam similar to the one in Figure 21. We consider the 15th mode shape of a $15'' \times 0.996'' \times 0.124''$ clamped–clamped copper beam with the $3''$ middle section having a thickness of $0.175''$. Figure 22 shows that, if the β is estimated to be the one of the two end segments, the SSD is zero for points on the two end segments. Moreover, the peaks and non-zero sections in Figures 22(b–d) clearly show the location of the stiffened segment. Figure 23 shows that, if the β is estimated to be the one of the middle segment, the SSD is zero for points on the middle segment. Moreover, the flat section of C_4 and $C_1 * C_3$ clearly show the location of the stiffened segment. Figure 24 shows the results of using the non-linear sliding-window least-squares fitting method shown in Appendix A to find the correct β for the three segments. The values of β are obtained to be 35.09 for the two end segments and 29.65 for the middle segment, which are actually the exact values. Hence, one can use this method to obtain the change of m/EI $(= \beta^4/\omega^2)$ in order to estimate the extent of damage. However, the peaks of $C_1 * C_3$ and the sign changes of C_4 in Figure 24 are close but not exactly at the ends of the middle segment.

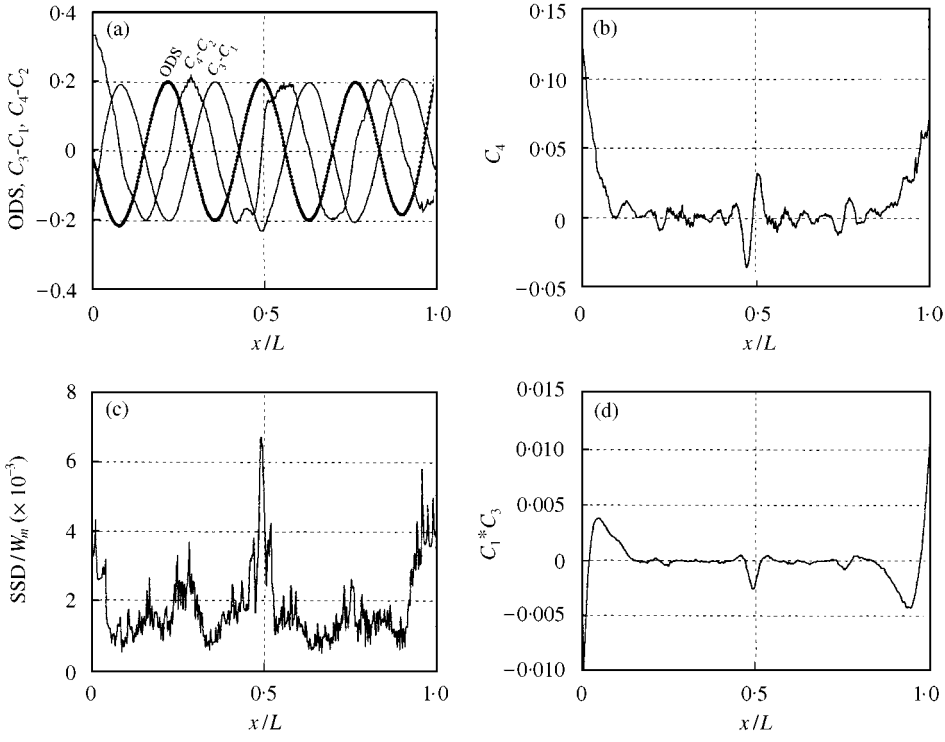

Figure 19. Experimental boundary effect detection of Cracks #1, #2, and #3 using the ODS corresponding to the eighth mode and $M = 400$, $N = 5$, and $\Delta x = 3L/400$: (a) ODS (dots), fitted ODS, $C_3 - C_1$, and $C_4 - C_2$, (b) C_4, (c) SSD/W_m, and (d) $C_1 * C_3$.

Moreover, it requires a large window length in order to have a converged value for β.

The experimental results of the beam in Figure 21 are shown in Figures 25–27. In the "FAST SCAN" acquisition, the PZT patch is excited by $100 \sin(8866\pi t)$ V, and the frequency bandwidth is chosen to be 4.433 Hz. The 15th natural frequency of the beam is 4433 Hz. Figures 25–27 show the results obtained by performing the analyses similar to those in Figures 22–24 respectively. Figure 25 uses the β of the two end segments, Figure 26 uses the β of the middle segment, and Figure 27 computes the β for every scanned point using the non-linear curve fitting. We use $N = 5$ and $\Delta x = 4L/250$ in Figures 25–27. We note that to smooth the β curve requires a window length larger than that for the *SSD* curve. The amplitude of the ODS is very small because the power amplifier used is not efficient at this frequency range. However, the non-zero part of C_4 in Figure 25(b), the zero part of $C_1 * C_3$ in Figure 26(b), the peaks of C_4 in Figure 27(b), and the area of small β in Figure 27(a) all show the end locations of the stiffened segment. Except for estimating damage extent by checking the change of β this non-linear curve-fitting method is not recommended because it requires more computation.

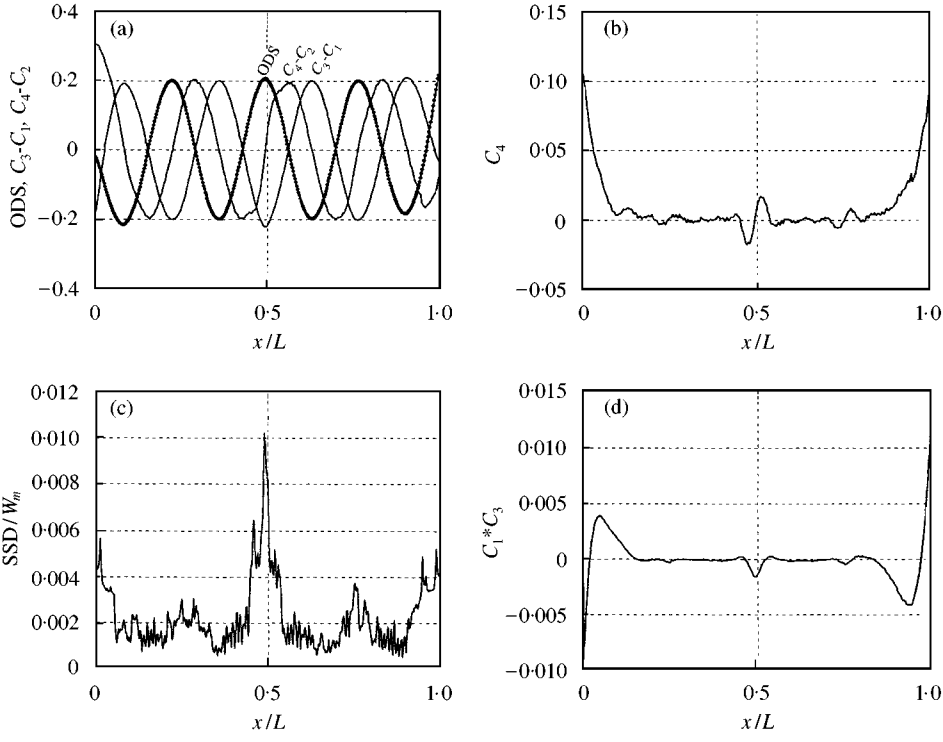

Figure 20. Experimental boundary effect detection of Cracks #1, #2, and #3 using the ODS corresponding to the eighth mode and $M = 400$, $N = 5$, and $\Delta x = L/100$: (a) ODS (dots), fitted ODS, $C_3 - C_1$, and $C_4 - C_2$, (b) C_4, (c) SSD/W_m, and (d) $C_1 * C_3$.

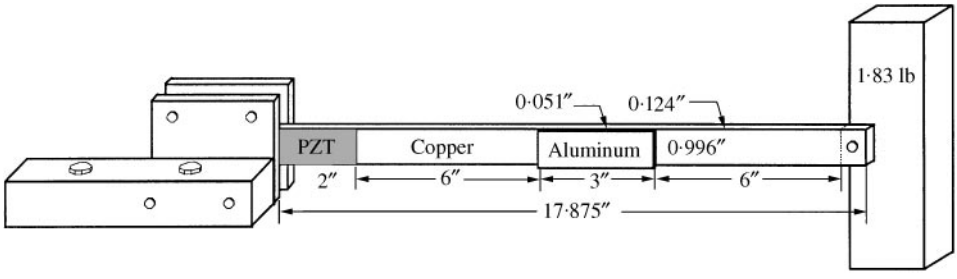

Figure 21. A cantilevered copper beam with a tip mass and a 3″ section stiffened by an aluminum segment.

Because the stiffened segment significantly reduces the curvature, it is similar to a large damage. Hence, low-frequency ODSs should also be able to show the "damage". Figure 28 shows that even the ODS corresponding to the first mode (40.3 Hz) can be used to locate the stiffened segment clearly. However, because

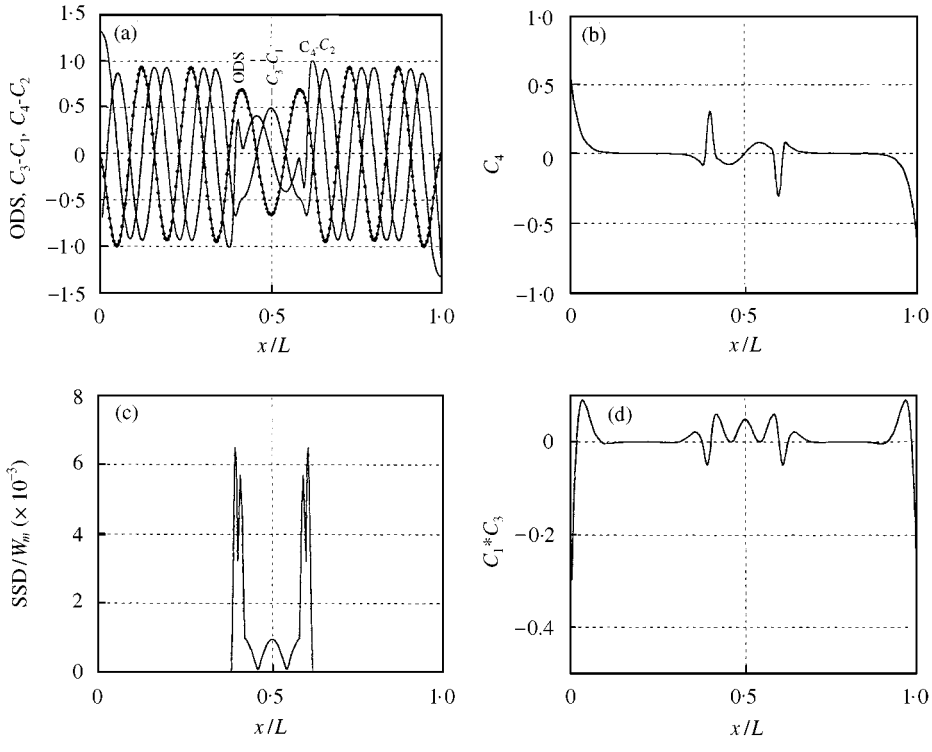

Figure 22. Numerical boundary effect detection of a 15″ clamped–clamped copper beam with a 3″ stiffened middle segment using the 15th mode shape without noise, the β of the two end segments, $M = 250$, $N = 5$, and $\Delta x = L/250$: (a) ODS (dots), fitted ODS, $C_3 - C_1$, and $C_4 - C_2$, (b) C_4, (c) SSD/W_m, and (d) $C_1 * C_3$.

low-frequency ODSs require a large window length to have smooth curves, the damage locations cannot be precisely located.

3.4. DISCUSSION

The presented numerical and experimental results show that each of the coefficients C_i and their combinations requires a different sliding-window length for curve fitting in order to smooth its curve. The required sliding-window length increases in the following order: (1) the difference of kinetic and elastic energy densities ($C_1 * C_3$), (2) the curvature ($C_3 - C_1$), (3) the central solution of slope (C_2), (4) the derivative of curvature ($C_4 - C_2$), (5) the boundary-layer solution of slope (C_4), (6) the fitting error (SSD), and (7) the β if the non-linear fitting is used. C_4, $C_1 * C_3$ and SSD are good at pinpointing damage. When the sliding-window length increases in the signal processing from a small value, $C_1 * C_3$ becomes smooth and can indicate the damage before $C_3 - C_1$ becomes smooth, and C_4 can still indicate the damage after $C_4 - C_2$ becomes too smooth to show damage. Moreover, this method can provide multiple indications of damage. Hence, this method is more

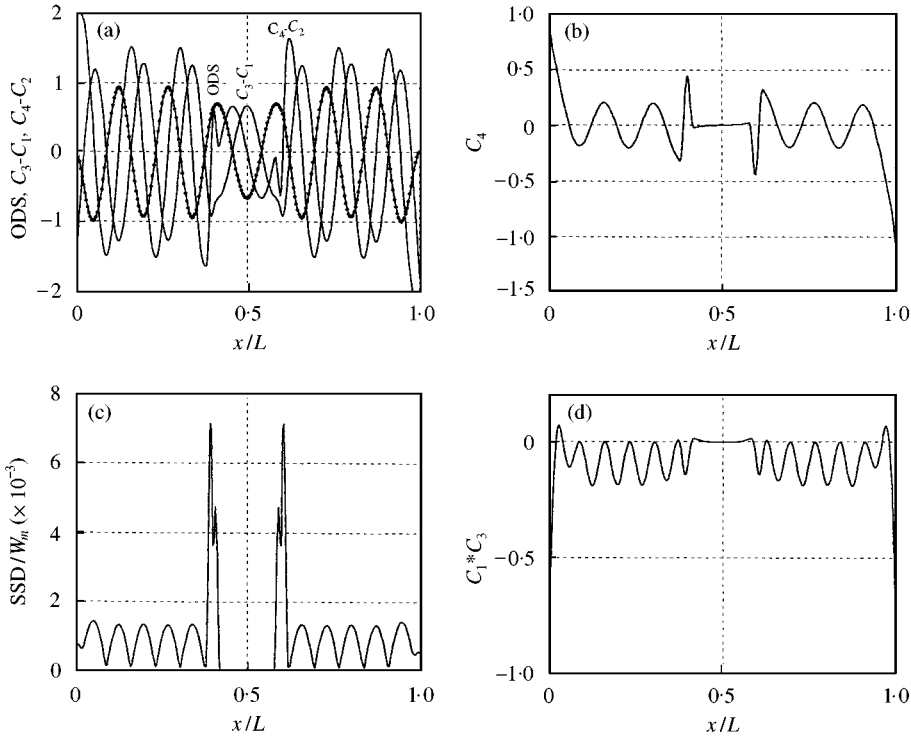

Figure 23. Numerical boundary effect detection of a 15″ clamped–clamped copper beam with a 3″ stiffened middle segment using the 15th mode shape without noise, the β of the middle segment, $M = 250$, $N = 5$, and $\Delta x = L/250$: (a) ODS (dots), fitted ODS, $C_3 - C_1$, and $C_4 - C_2$, (b) C_4, (c) SSD/W_m, and (d) $C_1 * C_3$.

reliable than damage identification methods using the change of W'' and W'''. More importantly, this method works without any historical data of the structure. However, if the measured area does not consist of uniform material, the intact ODSs of the structure need to be used for comparison in order to find new boundaries to locate damage.

The success of this method depends on the separation of boundary-layer solutions from the central solutions by using the proposed sliding-window curve-fitting method, and each of the coefficients obtained has a physical meaning. The accuracy of this method is controlled by (1) the noise contained in the ODSs, and (2) the length of $2N\Delta x$ of the sliding window used in the curve fitting. Because the noise level is proportional to the square root of the frequency bandwidth, one can use the following methods to reduce the noise in ODSs: (1) using the "FAST SCAN" acquisition to obtain ODSs instead of the "FFT" acquisition, (2) using small bandwidth in the "FAST SCAN" acquisition (down to 0.02% of the excitation frequency), (3) choosing the excitation frequency close to the isolated natural frequency to get a large vibration amplitude, and (4) using the "LOCK-IN AMPLIFIER" acquisition at the specific frequency.

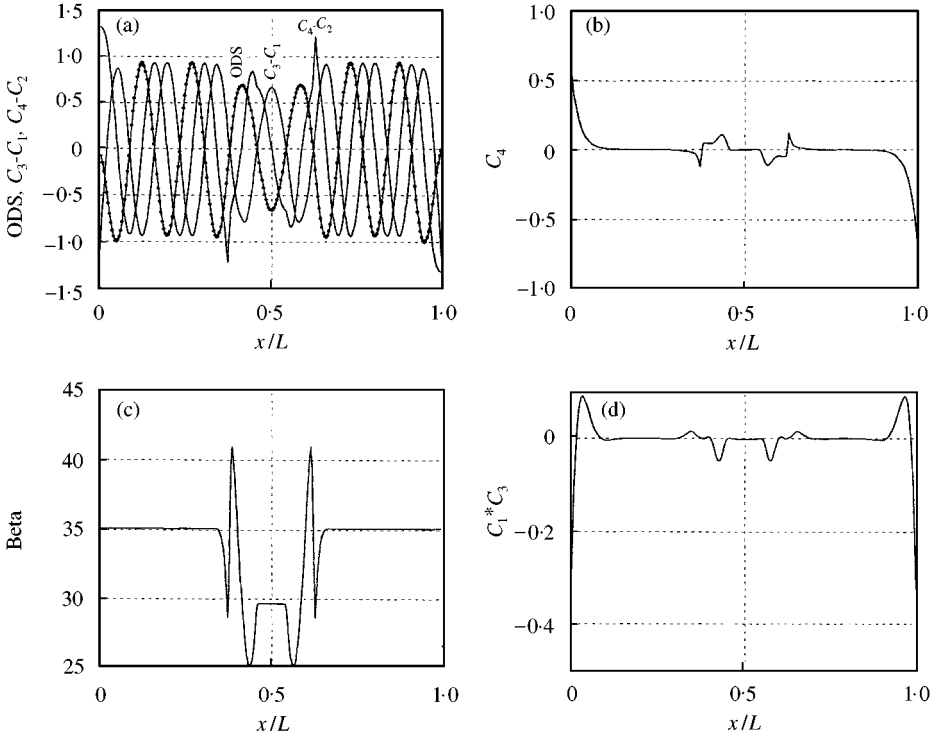

Figure 24. Numerical boundary effect detection of a 15″ clamped–clamped copper beam with a 3″ stiffened middle segment using the 15th mode shape without noise, the β obtained from non-linear curve fitting, $M = 250$, $N = 5$, and $\Delta x = 3L/250$: (a) ODS (dots), fitted ODS, $C_3 - C_1$, and $C_4 - C_2$, (b) C_4, (c) β, and (d) $C_1 * C_3$.

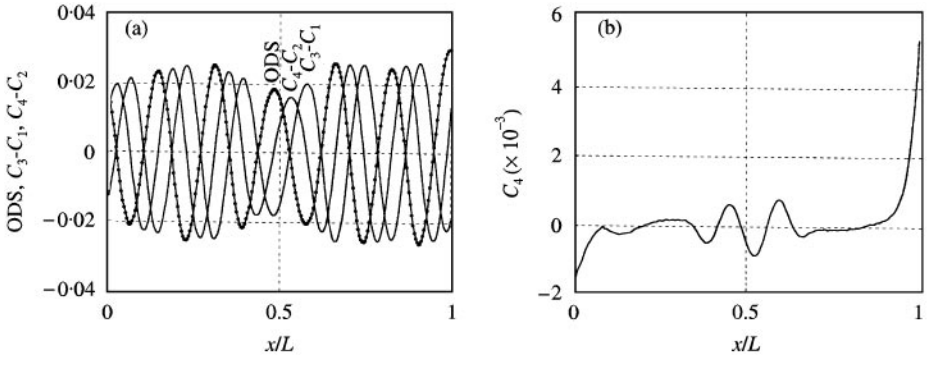

Figure 25. Experimental boundary effect detection of the beam in Figure 21 using the ODS corresponding to the 15th mode, the β of the two end segments, $M = 250$, $N = 5$, and $\Delta x = 4L/250$: (a) ODS (dots), fitted ODS, $C_3 - C_1$, and $C_4 - C_2$, and (b) C_4.

This boundary effect detection method works for beams with any boundary conditions. Moreover, this method can be extended by using eigenfunctions of plates/shells and a sliding-window least-squares surface-fitting method to locate damage to plates/shells, which is under current study.

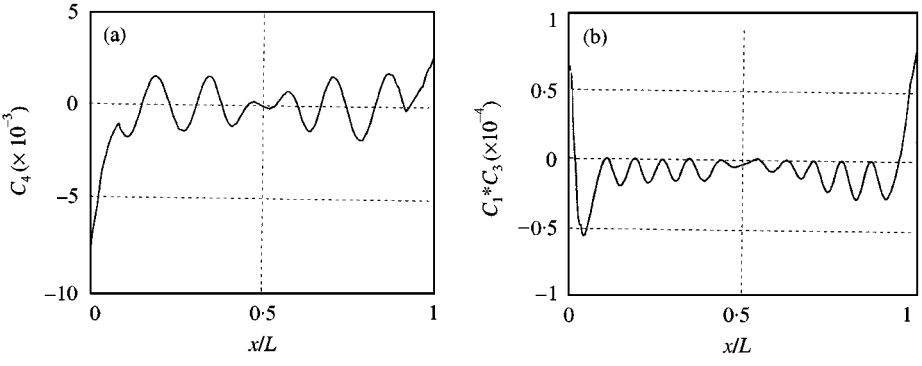

Figure 26. Experimental boundary effect detection of the beam in Figure 21 using the ODS corresponding to the 15th mode, the β of the middle segment, $M = 250$, $N = 5$, and $\Delta x = 4L/250$: (a) C_4, and (b) $C_1 * C_3$.

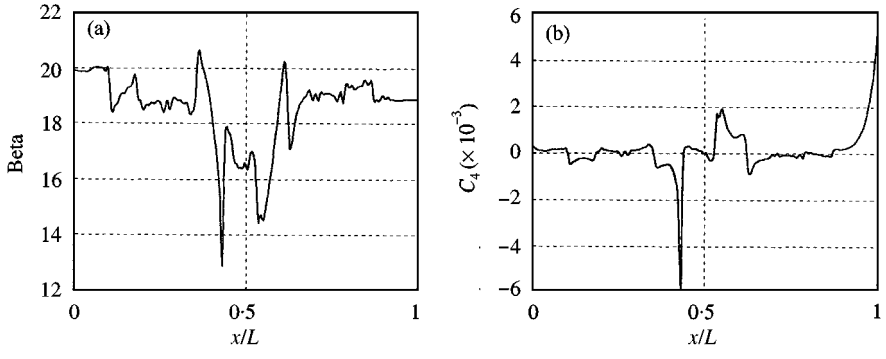

Figure 27. Experimental boundary effect detection of the beam in Figure 21 using the ODS corresponding to the 15th mode, the β obtained from non-linear curve fitting, $M = 250$, $N = 5$, and $\Delta x = 4L/250$: (a) β, and (b) C_4.

4. CONCLUSIONS

We present a method of locating structural damage using operational deflection shapes measured by a scanning laser vibrometer and a sliding-window least-squares curve-fitting technique. The method uses cos, sin, cosh, and sinh as trial functions to fit with the experimental operational deflection shapes. It is shown that coefficients of these trial functions have different physical meanings and they require different sliding-window lengths for curve fitting in order to obtain smooth curves. Based on the different sliding-window lengths required and peaks and sign changes of the coefficients we develop a boundary effect detection (BED) method for finding damage locations. Numerical and experimental studies on beams with different damages have been carried out to validate this method in locating small structural damages.

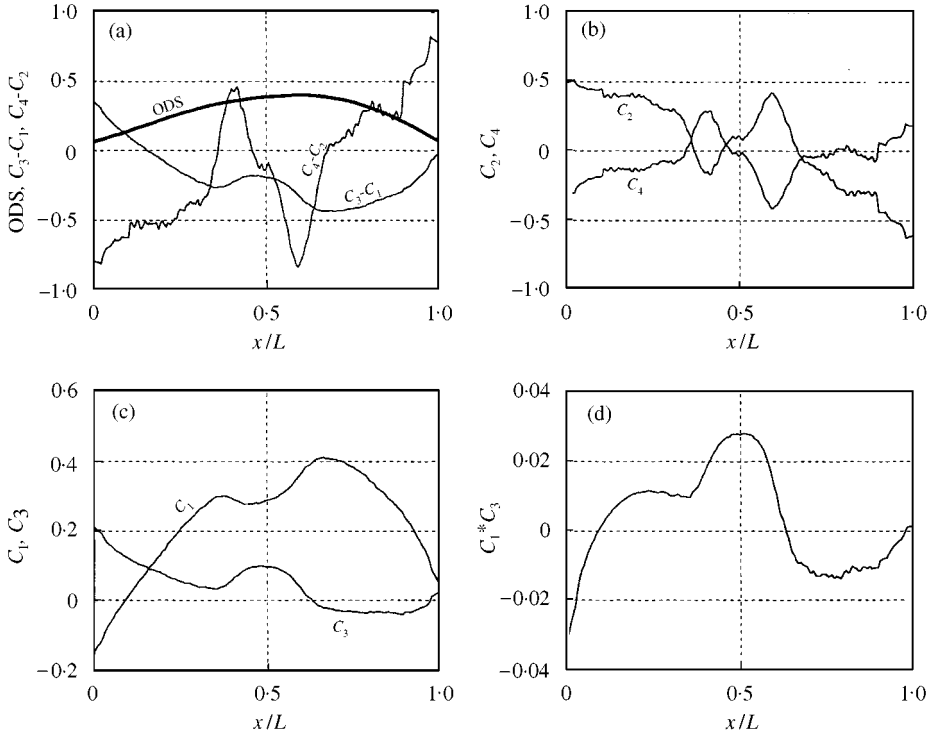

Figure 28. Experimental boundary effect detection of the beam in Figure 21 using the ODS corresponding to the first mode, the averaged β, $M = 250$, $N = 5$, and $\Delta x = L/50$: (a) ODS (dots), fitted ODS, $C_3 - C_1$, and $C_4 - C_2$, (b) C_2 and C_4, (c) C_1 and C_3, and (d) $C_1 * C_3$.

ACKNOWLEDGMENT

This work is supported by the National Science Foundation through Grant CMS-9871288. Dr. Shih-Chi Liu is the technical monitor. The support is gratefully acknowledged.

REFERENCES

1. S. W. Doebling, C. R. Farrar, M. B. Prime and D. W. Shevitz 1996 *Report No. LA-13070-MS, Los Alamos National Laboratory*. Damage identification and health monitoring of structural and mechanical systems from changes in their vibration characteristics: a literature review.
2. H. Zhang, M. J. Schulz, A. S. Naser, F. Ferguson, P. F. Pai, and J. Hurtado 1999 *Journal of Mechanical Systems and Signal Processing*. Structural health monitoring using transmittance functions (in press).
3. M. J. Schulz, A. S. Abdelnaser, P. F. Pai, M. S. Linvill and J. Chung 1997 *International Modal Analysis Conference, Orlando, FL, U.S.A.* Detecting structural damage using transmittance functions.
4. M. J. Schulz, A. S. Naser, P. F. Pai and J. Chung 1998 *Journal of Intelligent Material Systems and Structures* **9**, 899–905. Locating structural damage using frequency response reference functions.

5. H. T. Banks, D. J. Inman, D. J. Leo and Y. Wang 1996 *Journal of Sound and Vibration* **191**, 859–880. An experimentally validated damage detection theory in smart structures.
6. X. T. C. Man, L. M. McClure, Z. Wang and R. D. Finch 1994 *Journal of Acoustical Society of America* **95**, 2029–2037. Slot depth resolution in vibration signature monitoring of beams using frequency shift.
7. M. H. H. Shen and C. Pierre 1990 *Journal of Sound and Vibration* **138**, 115–134. Natural modes of Bernoulli–Euler beams with symmetric cracks.
8. J. Dugundji 1988 *AIAA Journal* **26**, 1013–1014. Simple expressions for higher vibration modes of uniform Euler beams.
9. D. Iesan 1987 *St. Venant's Problem*, Lecture Notes in Mathematics, Vol. 1279 (A. Dold and B. Eckmann, editors). New York: Springer.
10. V. Giavotto, M. Borri, P. Mantegazza, G. Ghiringhelli, V. Carmaschi, G. C. Maffioli and F. Mussi 1983 *Computers & Structures* **16**, 403–413. Anisotropic beam theory and applications.
11. W. T. Thomson 1949 *Journal of Applied Mechanics* **16**, 203–207. Vibration of slender bars with discontinuities in stiffness.
12. S. Christides and A. D. S. Barr 1984 *International Journal of Mechanical Science* **26**, 639–649. One-dimensional theory of cracked Bernoulli–Euler beams.
13. P. Cawley and R. D. Adams 1979 *Journal of Strain Analysis* **14**, 49–57. The location of defects in structures from measurements of natural frequencies.
14. D. J. Inman 1994 *Engineering Vibration*. Englewood Cliffs, NJ: Prentice-Hall.
15. Active Control eXperts, Inc., Cambridge, MA.

APPENDIX A: NON-LINEAR SLIDING-WINDOW LEAST-SQUARES CURVE-FITTING METHOD

Here we describe the non-linear sliding-window least-squares method. If f denotes the difference between the curves-fitted operational deflection shape $W(\bar{x})$ shown in equation (7) and the experimental operational deflection shape $Y(\bar{x})$, we have

$$f(C_1, C_2, C_3, C_4, \beta) = C_1 \cos(\beta\bar{x}) + C_2 \sin(\beta\bar{x}) + C_3 \cosh(\beta\bar{x}) + C_4 \sinh(\beta\bar{x}) - Y(\bar{x}),$$

where $\bar{x} \equiv x - x_m$ and x_m is the location of the observed point. To find the increments ΔC_i and $\Delta\beta$ in order to update C_i and β to minimize f we perform the Taylor expansion of f as

$$\hat{f} = f + \frac{\partial f}{\partial C_1}\Delta C_1 + \frac{\partial f}{\partial C_2}\Delta C_2 + \frac{\partial f}{\partial C_3}\Delta C_3 + \frac{\partial f}{\partial C_4}\Delta C_4 + \frac{\partial f}{\partial \beta}\Delta\beta. \tag{A.1}$$

Then we define an error function $\hat{E}_{rror}$ as

$$\hat{E}_{rror} = \sum_{i=-N}^{N} \alpha_i \hat{f}_i^2, \tag{A.2}$$

where $\hat{f}_i \equiv \hat{f}(\bar{x}_i)$ and α_i is the same weighting factor as that used in equation (8). The five equations to determine ΔC_i and $\Delta\beta$ are given by

$$\frac{\partial \hat{E}_{rror}}{\partial \Delta\beta} = \frac{\partial \hat{E}_{rror}}{\partial \Delta C_i} = 0, \quad i = 1, 2, 3, 4. \tag{A.3}$$

One can solve these five equations to obtain ΔC_i and $\Delta\beta$. Keep updating C_i and β to minimize $\hat{E}_{rror}$ until $\Delta\beta$ is less than $\varepsilon(\ll 1)$ of the previous β.